Research Article

Seham S. Alterary*, Muntaha S. Aldaoud and Manal A. Awad*

Optical, structural, and morphological characterization of hydrothermally synthesized zinc oxide nanorods: exploring their potential for environmental applications

https://doi.org/10.1515/ntrev-2025-0257
Received June 17, 2025; accepted November 30, 2025;
published online December 25, 2025

Abstract: This study presents the synthesis and multifunctional evaluation of nanostructured zinc oxide nanorods (ZnO NRs) using a hydrothermal method. Various characterisation techniques, including X-ray diffraction (XRD), Fourier transform infrared spectroscopy (FTIR), ultraviolet–visible (UV–vis) spectrometry, fluorescence spectroscopy, energy-dispersive X-ray spectroscopy (EDS), transmission electron microscopy (TEM), and X-ray photoelectron spectroscopy (XPS), were employed to analyse the ZnO NRs. XRD analysis confirmed the hexagonal wurtzite structure of the ZnO NRs. FTIR spectra showed a characteristic peak near 873 cm^{-1} corresponding to Zn–O stretching and out-of-plane C–H bending vibrations, indicating surface interactions. UV–vis analysis revealed strong absorption in the UV region and high optical transparency in the visible range, while the Tauc plot determined bandgaps of 3.29 ± 0.03 eV and 3.66 ± 0.01 eV, which enhance electron transfer processes during photocatalysis. The fluorescence spectrum displayed a sharp emission peak at 340 nm, attributed to near-band-edge emission and quantum confinement effects. SEM and TEM micrographs showed well-dispersed, rod-like nanoparticles with an average width of 47.7 nm. EDS confirmed high purity with 60 % Zn and 20 % O, while XPS verified the successful incorporation of ZnO within the thin-film coating. The ZnO NRs demonstrated strong photocatalytic performance in degrading crystal violet (CV) dye under solar light, achieving over 95 % ± 0.01 degradation with a rate constant of 0.6767 min^{-1}. Hydrophobicity testing using a contact angle goniometer revealed a contact angle of 95.6° ± 0.3, indicating potential self-cleaning properties. XPS analysis further confirmed the presence of ZnO NRs within the thin-film coating and validated their successful incorporation. These findings collectively highlight the effectiveness of ZnO NRs in photocatalytic and surface coating applications, suggesting their promising potential for environmental and industrial use.

Keywords: hydrothermal synthesis; ZnO NRs; environmental applications

1 Introduction

In recent years, nanotechnology has become one of the most rapidly advancing fields in science and technology, driving significant innovations across multiple disciplines. Nanomaterials, defined by their unique physicochemical properties, have enabled the development of novel systems, structures, devices, and nanoplatforms with broad applications [1, 2]. These materials exist at the nanoscale, exhibiting superior thermal conductivity, catalytic reactivity, optical performance, and chemical stability due to their high surface area-to-volume ratio [3]. This distinctive property has motivated extensive research into new synthesis techniques for nanomaterials [4]. Among various nanomaterials, semiconductor-based photocatalysts have attracted considerable attention due to their potential to address critical environmental challenges, particularly water pollution [5]. Industrial dye effluents, mainly from textile and dye manufacturing industries, contribute significantly to global water contamination. Consequently, self-cleaning surfaces and photocatalytic materials have emerged as promising solutions [6]. Among semiconductor photocatalysts, zinc oxide nanoparticles (ZnO NPs) have been

***Corresponding authors: Seham S. Alterary**, King Abdullah Institute of Nanotechnology, King Saud University, Riyadh 11451, Saudi Arabia; and Department of Chemistry, College of Science, King Saud University, Riyadh 11451, Saudi Arabia, E-mail: salterary@ksu.edu.sa. https://orcid.org/0000-0002-4176-2840 (S.S. Alterary); and **Manal A. Awad**, King Abdullah Institute of Nanotechnology, King Saud University, Riyadh 11451, Saudi Arabia, E-mail: mawad@ksu.edu.sa. https://orcid.org/0000-0002-5294-1721 (M. A. Awad)
Muntaha S. Aldaoud, Department of Chemistry, College of Science, King Saud University, Riyadh 11451, Saudi Arabia, E-mail: muntahaaldaoud01@gmail.com

extensively studied due to their unique optoelectronic and physicochemical properties, making them suitable for diverse applications [7].

Photocatalytic degradation, which uses semiconductor metal oxides to decompose persistent organic pollutants in wastewater, has proven to be a highly efficient approach to water purification. This technique harnesses visible light and does not require sophisticated infrastructure, making it a cost-effective and sustainable method for environmental remediation. ZnO-based photocatalysts, serving as both active catalysts and self-cleaning coatings, have demonstrated exceptional efficiency in degrading hazardous organic dyes in contaminated water and on various surfaces [8, 9]. Nanostructured photocatalytic materials, including titanium dioxide (TiO_2) [10, 11], ZnO [12], and carbon-based nanomaterials [13], have been extensively explored for environmental applications. In particular, ZnO has attracted significant research interest due to its low cost, high redox potential, abundance, non-toxicity, and eco-friendly nature. Its strong ultraviolet (UV) absorption, wide bandgap (3.37 eV), excellent biocompatibility, thermal stability, and antimicrobial properties further enhance its potential for various applications. ZnO nanostructures can be synthesised with diverse morphologies, such as nanowires, nanotubes, nanosheets, nanoplumes, and nanorods, using different fabrication techniques, including sol-gel, hydrothermal, electrodeposition and green chemistry methods [14–17]. Despite its promising photocatalytic properties, ZnO has limitations, including rapid electron–hole recombination, which reduces its efficiency under visible-light irradiation. To address this challenge, researchers have explored several strategies to enhance its photocatalytic performance. Qi et al. [12] investigated modifications such as metal and non-metal doping, heterojunction formation, carbon nanostructure integration, and noble metal incorporation. For example, Ag doping has been shown to enhance the photocatalytic oxidation of both anionic and cationic dyes using Ag@ZnO nanocomposites under UV irradiation [18, 19]. ZnO is inherently hydrophobic; however, its surface properties can be tailored to achieve superhydrophobicity using low-surface-energy materials such as fluorosilane, stearic acid, noctadecanoic acid, and polydimethylsiloxane [20]. Gao et al. [21] developed superhydrophobic ZnO surfaces capable of efficiently separating oil–water mixtures, while Nundy et al. [22] synthesised morphologically distinct hydrophobic ZnO microstructures without UV treatment, demonstrating their potential for self-cleaning applications in photovoltaic and glazing technologies. Recent research has also emphasised ZnO-based composites and metal-doped systems to improve photocatalytic and electrochemical performance. Pramod Agale et al. [12] reported Sr-doped ZnO@g-C_3N_4 nanocomposites exhibiting enhanced charge carrier dynamics and notable potential in energy storage, photocatalysis, and environmental remediation. Similarly, Zarina Ansari et al. [14] synthesised Mn-doped ZnO@rGO nanocomposites with superior electrochemical and photoelectrochemical behaviour, highlighting their applicability in supercapacitor and photoelectrochemical (PEC) systems.

Despite these advances, few studies have explored the interplay between ZnO nanostructure morphology, optical properties, and multifunctional performance – particularly the integration of hydrophobicity with photocatalytic activity. The present study aims to address this gap by synthesising ZnO nanorods (ZnO NRs) via a hydrothermal route and systematically investigating their structural, optical, and surface characteristics. Furthermore, this work focuses on evaluating their self-cleaning behaviour and photocatalytic degradation efficiency using crystal violet (CV) dye as a model pollutant. CV was specifically chosen due to its carcinogenic nature and resistance to degradation, making it an ideal compound for assessing photocatalytic performance under solar irradiation.

2 Materials and methods

2.1 Hydrothermal synthesis of ZnO NRs

Zinc oxide nanorods (ZnO NRs) were synthesised using the modified method described by Nundy et al. [22]. First, 1.1899 g of NaOH was dissolved in 25 ml of distilled water with a magnetic stirrer until fully dissolved. An ice bath was prepared for the NaOH solution, and 0.09 g of cetyltrimethylammonium bromide (CTAB) was added while stirring, then left to stand for 5 min. Next, 946.8 mg of zinc nitrite ($Zn(NO_2)_2$) was added to the mixture, with continuous stirring for 1 h.

After complete dissolution, the solution was transferred to an autoclave and placed in an oven at 80 °C for 6 h to promote the dissolution–recrystallisation process, enhancing the crystallinity and aspect ratio of the ZnO nanorods [22]. After cooling, the sample was centrifuged to precipitate the nanoparticles, followed by three wash cycles with ethanol and distilled water. Each washing step lasted 30 min at 10,000 rpm. The resulting white precipitate was collected and dried in a hot air oven for 10 h at 80 °C. Finally, the powder was calcined at 400 °C for 3 h.

2.2 Characterization of synthesized samples

The optical properties of the synthesised ZnO NRs were investigated using a UV-1800 UV–vis spectrometer (Shimadzu, Switzerland) in the range 200–600 nm. The bandgap

energy (Eg) was determined by the Tauc plot method. The emission spectrum and fluorescence (FL) were measured with a Fluorolog 3 spectrofluorometer (FL-3-11, Horiba JobinYvon, Edison, NJ, USA). The crystalline structures and average particle sizes were analysed using a Bruker D8 ADVANCE X-ray diffractometer (Bruker, Billerica, MA, USA) at 40 kV and 40 mA with CuKα radiation at 1.5418 Å. The surface morphology and size of the nanoparticles were examined using TEM with an accelerating voltage of 200 kV (JEM-2100F, JEOL Ltd., Peabody, MA, USA). An energy-dispersive X-ray spectrometer (EDS, JSM-2100F, JEOL, USA) connected to the SEM (JEOL JSM-7600F, USA) was used for elemental identification and mapping in the ZnO powder. Functional groups on the surface of the ZnO NRs, in the CV dye, and in the treated CV dyes were identified using a Fourier transform infrared (FTIR) spectrometer (Shimadzu IR, Prestige 21, Nakagyo-Ku, Kyoto, Japan) covering the range 4,000–400 cm^{-1}. The chemical composition of the surface was analysed using X-ray photoelectron spectroscopy (XPS) (Jeol JPS-9200 photoelectron spectrometer) with a 500 W X-ray source (JEOL Ltd., Akishima, Tokyo, Japan).

2.3 Experiment on self-cleaning surfaces

To prepare the self-cleaning surface, glass slides were meticulously cleaned to remove contaminants. The slides were immersed in a 10 % sulfuric acid (H_2SO_4) solution for 15 min, and then thoroughly rinsed with distilled water and acetone to achieve a pristine surface. For the coating preparation, a ZnO NR solution was formulated using polymethyl methacrylate (PMMA) as a binder to enhance adhesion. The PMMA (in pellet form, provided by SABIC, Saudi Arabia; density: 1.20 g/cm^3, SABIC® PMMA) was dissolved in toluene (99.8 %, Sigma) as the solvent. Specifically, 1.5 mg of ZnO NR powder was dispersed in 20 ml of a PMMA solution (0.5 mg/ml) to ensure uniform distribution. The dispersion was carried out using an ultrasonicator (750 W, 20 kHz) for 1 h. The coating solution was then applied to the cleaned glass slides using the spin-coating technique. To achieve a homogeneous thin film with adequate thickness, a two-step spin-coating cycle was employed for each sample: first, a spread cycle at 500 rpm for 10 s, followed immediately by a high-speed cycle at 2,000 rpm for 30 s. This two-step cycle was repeated three times to build the film layer by layer. After each coating cycle, the slides were dried at 45 °C for 5 min in an oven to partially evaporate the solvent. After the final coating cycle, the slides underwent a final drying step at 45 °C for 15 min to ensure complete solvent removal and film consolidation, before being cooled to room temperature, following established protocols [23]. To evaluate the surface wettability of the ZnO NR-coated glass slides, water contact angle (WCA) measurements were conducted using the sessile drop method with Dataphysics OCA15EC equipment (Stuttgart, Germany). A 5 µl droplet of deionised water was carefully deposited onto the coated surface using a microsyringe, and the contact angle (θ) at the liquid–solid interface was recorded. To ensure accuracy and reliability, WCA measurements were performed three times for each sample, and the average value was calculated and reported in the analysis.

2.4 Photocatalysis activity studies

In this experimental investigation, a rigorous protocol was implemented to assess the photodegradation efficacy of zinc oxide nanoparticles (NPs) on crystal violet (CV) dye. Initially, 100 ml of distilled water was thoroughly mixed with 1 ppm of CV dye until fully dissolved. The dye solution was then placed in a glass vessel, and a predetermined amount of catalyst was added. Simultaneously, another sample was taken immediately after the introduction of the nanoparticles to serve as the “time zero” reference.

The mixture was then exposed to solar irradiation outdoors. This exposure to sunlight occurred daily for 3 h over a five-day period, from 25 to 29 May 2023. The experimental conditions simulated a relatively hot climate, with peak temperatures ranging from 35 to 37 °C and lows between 25 and 28 °C. At specified intervals, approximately 5 ml aliquots were withdrawn and allowed to settle to prevent potential interference from the catalyst. Additional samples were systematically collected, and the entire procedure was repeated three times to ensure the robustness of the experimental results. Dye degradation was assessed using a UV-visible spectrometer for all collected samples, with distilled water as the blank reference. This approach provides a comprehensive understanding of the impact of ZnO NRs on CV dye under real-world environmental conditions. The removal percentage (%) was calculated using the following formula:

$$\text{Removal percentage } (\%) = \left[\text{Co} - C/\text{Co} \times 100\right] \quad (1)$$

C_0 represents the initial concentration of crystal violet dye, while C denotes the crystal violet dye concentration at various time intervals. The experiment was repeated three times to ensure consistency, enhancing the reliability and comprehensiveness of the investigation into the impact of ZnO NRs on CV dye under real-world environmental conditions.

2.5 Statistical analysis

The data were statistically analysed using one-way analysis of variance (ANOVA) and Tukey's post hoc test with Origin 2019b software (version 9.65 for Windows, Ontario, Canada). For each experiment, the data are presented as the mean ± standard deviation (SD) of three independent experiments.

3 Result and discussion

3.1 XRD pattern analysis of ZnO NRs

The distinctive X-ray diffraction (XRD) pattern of the hydrothermally synthesised ZnO NRs is shown in Figure 1, revealing characteristic peak values consistent with standard data for ZnO NRs. The XRD analysis, in accordance with JCPDS card number COD 9008877, assigns all diffraction peaks to the wurtzite structure of ZnO, with lattice parameters $a = b = 3.24950$ nm and c = 5.20690 nm. Notably, diffraction peaks at 2θ = 31.773°, 34.420°, 36.256°, 47.540°, 56.600°, 62.856°, 66.383°, 67.951°, 69.091°, 81.380°, and 92.811° were observed, corresponding to the (1 0 0), (0 0 2), (1 0 1), (1 0 2), (2 1 0), (1 0 3), (2 0 0), (2 1 2), (2 0 1), (1 0 4), and (3 1 0) crystallographic planes, respectively. The strong and sharp nature of these peaks indicates excellent crystallinity, highlighting the characteristic diffractions of the hexagonal wurtzite ZnO structure [24, 25]. The absence of significant impurity peaks demonstrates the high purity of the synthesised ZnO NRs. The average crystallite diameter of ZnO NRs was calculated using Scherrer's formula [26]. According to the XRD data, the ZnO NRs had an average crystallite size of approximately 22 nm. This comprehensive XRD analysis provides important insights into the structural characteristics and purity of the synthesised ZnO nanorods.

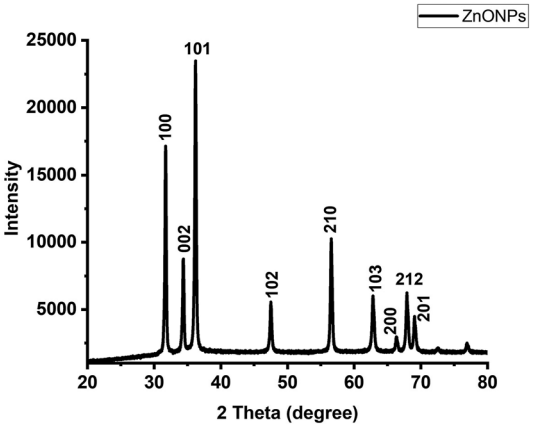

Figure 1: The XRD analysis results of ZnO NRs.

3.2 FTIR spectrum analysis of ZnO NRs

The FTIR spectrum of ZnO nanorods is illustrated in Figure 2, highlighting significant variations associated with the presence or absence of –OH groups The synthesized ZnO nanorods exhibit a characteristic Zn–O stretching vibration, typically observed around 546 cm^{-1}. The broad absorption peak centered at 3419 cm^{-1} corresponds to the stretching vibrations of O–H groups on the ZnO NR surface, indicating surface hydroxylation [27]. Additionally, the FTIR spectrum reveals distinct peaks at approximately 873 cm^{-1} and 1620 cm^{-1}. The peak at 873 cm^{-1} is typically attributed to out-of-plane bending vibrations of C–H bonds or Zn–O stretching, suggesting possible interactions between the ZnO nanorods and surface-adsorbed species. Furthermore, it may indicate the presence of carbonate species adsorbed onto the surface. The peak at 1620 cm^{-1} corresponds to the bending vibration of adsorbed water molecules (H–O–H bending) or the stretching vibration of C=O groups, which could originate from atmospheric moisture or residual precursor components. Additionally, the peaks observed around 2800 cm^{-1} correspond to C–H stretching vibrations, likely arising from residual precursor molecules that remained or evaporated during the synthesis process [28].

3.3 UV-Visible absorption spectrum analysis

UV–visible absorption spectroscopy was used to investigate the optical properties of the synthesised ZnO nanorods. As shown in Figure 3, the absorption spectrum displays two prominent peaks at 336 nm and 370 nm, characteristic of the

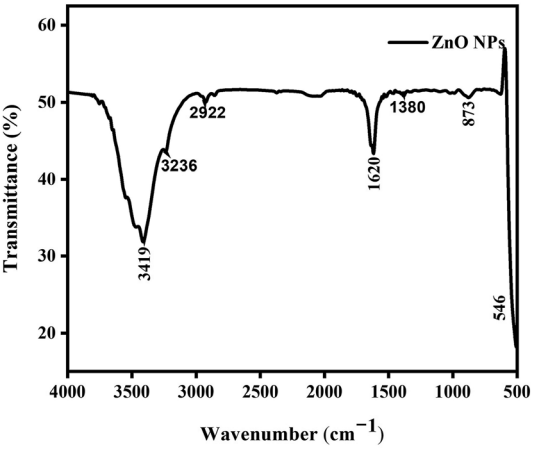

Figure 2: The FTIR spectrum of ZnO NRs.

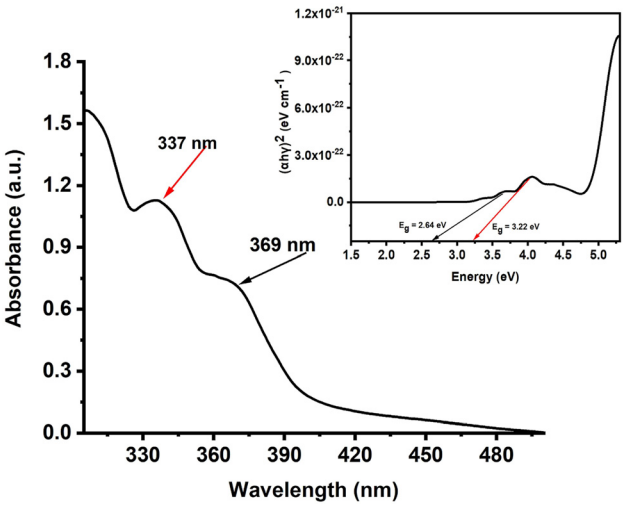

Figure 3: Presents the UV-visible spectrum of the synthesized ZnO NRs, showcasing three distinct absorption peaks along with their corresponding band gaps.

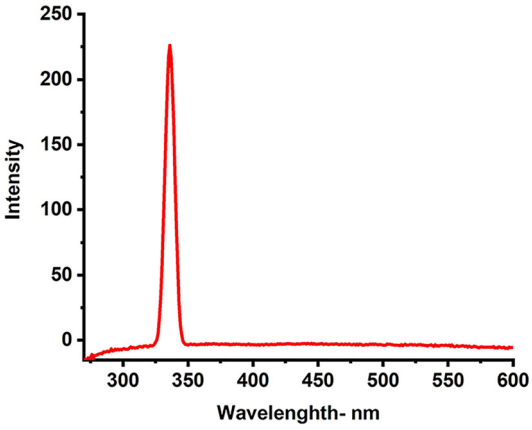

Figure 4: Fluorescence spectrum of ZnO nanorods.

hexagonal wurtzite structure of ZnO [29–31]. These two distinct absorption features correspond to electronic transitions within the material, providing insight into its structural and optical behaviour [31]. The optical bandgaps were estimated from Tauc plots [17], yielding values of 3.66 ± 0.01 eV and 3.29 ± 0.03 eV. The higher bandgap (3.66 eV), associated with the 336 nm peak, is attributed to excitonic absorption and possible defect-related transitions, where bound electron-hole pairs or lattice imperfections create discrete energy states [32, 33]. The lower bandgap (3.29 eV), linked to the 370 nm peak in the UV-A region, is commonly associated with oxygen vacancies or impurity-induced states within the band structure. Such vacancies, which are abundant in ZnO, play a key role in tuning its optical response. The coexistence of these two bandgaps is advantageous, as it can enhance electron transfer processes and thus facilitate applications such as photocatalytic dye degradation [34]. Variations in peak position and intensity may result from differences in particle size, morphology, synthesis conditions, or the presence of surface states and dopants. Careful analysis of these spectral features is therefore essential for understanding the electronic structure and optical performance of ZnO nanomaterials, which underpin their applications in photocatalysis, sensors, and optoelectronic devices [35, 36].

3.4 Fluorescence spectrum analysis of ZnO NRs

In Figure 4, the fluorescence spectrum of ZnO NRs shows a distinct emission peak at 340 nm, which may be attributed to near-band-edge emission, potentially influenced by quantum confinement effects or excitonic transitions [37, 38]. The sample exhibited strong fluorescence with no noticeable quenching. When the excitation wavelength was increased beyond 300 nm, a red shift in the emission peak was observed, along with a decrease in fluorescence intensity [39, 40]. The modest shift in both fluorescence peak position and intensity can be attributed to enhanced crystallinity and controlled vacancy formation within the nanoparticles. The absence of fluorescence quenching suggests high crystallinity, indicating minimal non-radiative recombination and controlled defect states. The correlation between this finding and the UV–vis absorption results of ZnO NRs lies in their shared dependence on the material's electronic structure, defect states, and crystallinity [36].

3.5 Elemental composition and TEM analysis of ZnO NRs

The elemental composition of the synthesised ZnO nanorod photocatalyst was assessed using EDS analysis. In Figure 5A, the EDS results confirm the presence of signals corresponding to zinc and oxygen, which are characteristic of zinc oxide nanoparticles. The analysis also identified peaks related to the optical absorbance of the synthesised nanoparticles [41]. The elemental composition of the nanoparticles revealed approximately 60 % zinc and 20 % oxygen, indicating a high level of purity in the synthesis process. Traces of carbon (13 %) and sodium (7 %) were also detected, which may have been introduced during the washing step of the synthesis. This finding is consistent with the FTIR results, confirming the presence of characteristic functional groups such as hydroxyl (–OH) and carbonate species. These functional groups correspond to the elemental composition detected by EDS,

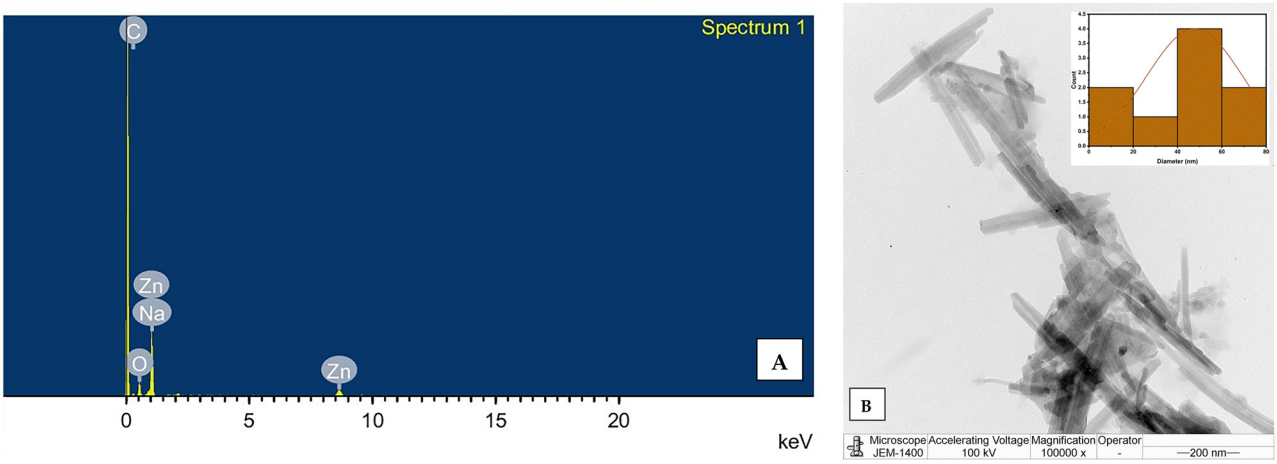

Figure 5: Elemental composition and structural morphology of ZnO NRs: (A) EDS spectrum confirming the elemental composition of ZnO NRs; (B) TEM micrographs with particle size distribution of ZnO NRs.

particularly the presence of oxygen and carbon. The Zn–O stretching vibration observed in the FTIR further supports the presence of Zn and O elements identified by EDS.

TEM analysis was used to characterise the surface morphology of the synthesised ZnO NRs. In Figure 5B, a typical TEM image of the synthesised ZnO NRs shows the prevalence of rod-shaped particles, with some particles aggregating into rods. The particle size distribution of the synthesised ZnO NRs was determined using ImageJ software. Figure 5B illustrates the formation of rods with varying widths and lengths. Notably, the absence of rod branching indicates the spontaneous nucleation of ZnO nanorods with high crystal perfection [42]. The nanorod-shaped particles have a width of 47.7 nm, confirming the formation of nanoscale ZnO. Shakee N. et al. reported a strong correlation between nanorod morphology and enhanced photocatalytic performance. The one-dimensional (1D) rod-like structure of ZnO provides a high aspect ratio and directional pathways for charge transport, which significantly suppress electron–hole recombination. In addition, the exposed polar facets of the hexagonal wurtzite structure, particularly the (0001) planes, act as highly active sites for dye adsorption and the generation of reactive oxygen species under solar irradiation. Furthermore, the uniform alignment and high crystallinity of ZnO nanorods enhance light absorption, promote efficient charge separation, and increase surface–reactant interactions. Collectively, these structural and morphological features account for the superior photocatalytic efficiency of ZnO NRs [43].

3.6 XPS spectrum analysis of ZnO NR thin film

X-ray photoelectron spectroscopy (XPS) was used to investigate the chemical states of elements and functional groups in the ZnO nanorod coating solution applied to the glass slides. The XPS spectra confirm the presence of oxygen and carbon in the samples, as indicated by peaks at approximately 284.9 eV and 533.7 eV, corresponding to the C 1s and O 1s electrons, respectively (Figure 6). The XPS spectrum also shows two distinct peaks for zinc: Zn $2p_3/_2$ at around 1,021 eV and Zn $2p_1/_2$ at around 1,044 eV (Figure 6) [44]. These peaks indicate the presence of ZnO nanorods within the PMMA matrix of the thin film coating on the glass slides, further confirming the incorporation of ZnO nanorods into the coating.

3.7 Transmittance spectrum analysis of ZnO NRs

The light transmittance of the ZnO NR sample, synthesised and evaluated across the 200–800 nm wavelength range (as shown in Figure 7), exhibited high transparency in the visible region and clear absorption in the UV region. The transmittance reached nearly 100 % between 400 and 800 nm, with a substantial decrease observed near 400 nm (~65 %), followed by a complete decline beyond 300 nm. This pronounced reduction in transmittance in the UV range compared to the visible range highlights the inherent UV-light absorption capability of ZnO NRs. These optical properties are consistent with previous literature, confirming ZnO's well-established behaviour as a material with high transparency in the visible spectrum and effective UV-blocking properties [45]. This finding supports the potential of ZnO NRs as an effective component in self-cleaning coatings for windows, solar panels, and building exteriors. Furthermore, the high transparency in the visible spectrum

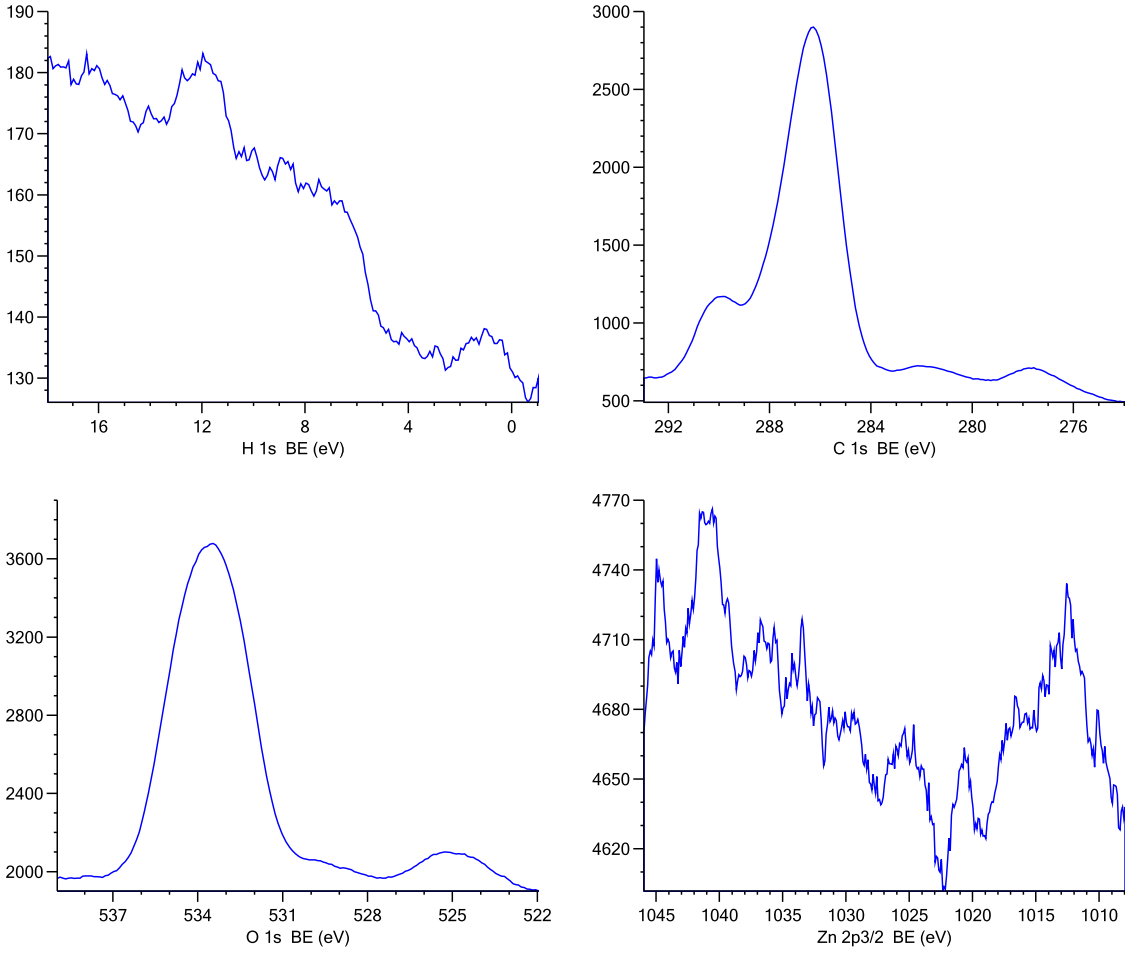

Figure 6: The wide XPS spectrum shows Zn 2p, C 1s, and O 1s peaks of the thin film-coated glass slide.

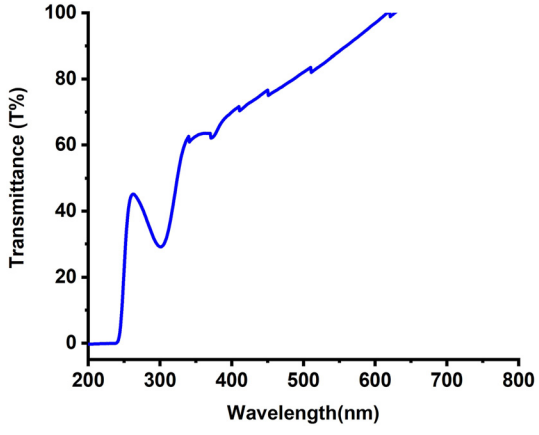

Figure 7: Illustrates the light transmittance (%) spectrum of the synthesized ZnO NRs.

allows ZnO-based coatings to be applied to glass surfaces without compromising optical clarity, enhancing their practicality for real-world applications.

3.8 Contact angle measurement for self-cleaning analysis of ZnO NRs

Contact angle (CA) measurements were carried out using a 5 µL water droplet at ambient temperature. Figure 8A shows the water droplet before and after contact with the ZnO NRs-coated surface. The CA value was measured as 95.6° ± 0.3, confirming the hydrophobic nature of the surface, while Figure 8B illustrates the actual droplet shape. The high contact angle is attributed to the structural characteristics of the ZnO NRs, which form a rod-like assembly both within the PMMA matrix and on the glass surface. The PMMA matrix plays a key role in enhancing the durability of the ZnO NR-based hydrophobic coating. Embedding the nanorods within PMMA provides mechanical stability, improves adhesion to the glass substrate, and reduces the likelihood of detachment during handling or exposure to water. The polymer matrix also prevents nanorod agglomeration and minimises surface wear, thereby supporting the long-term retention of hydrophobicity. In addition, PMMA offers excellent transparency

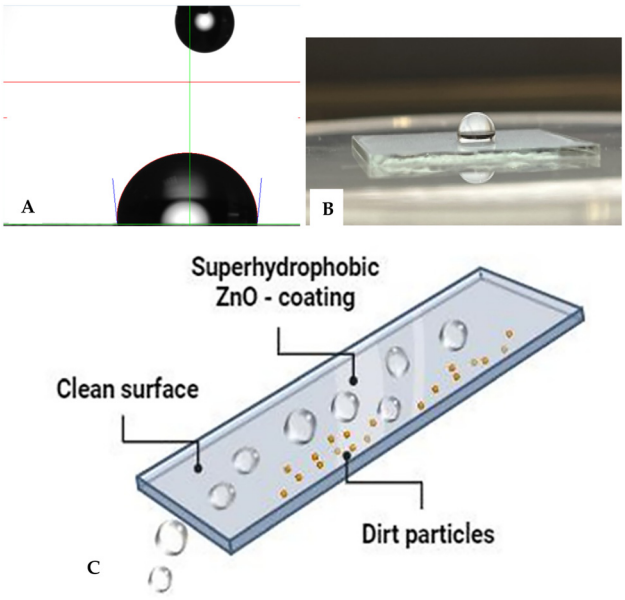

Figure 8: Water droplet contact angle measurement: (A) water drop before coming into contact with the surface and after coming into contact with the film of ZnO NRs-PMMA coated glass substrate, while (B) is represents the photograph of water drop on film of ZnO NRs – PMMA coated glass substrate, (in supplementary file see the video of video of water drops sliding without getting the glass slide coated with the hydrophobic film wet.), (C) illustrates the schematic representation of the hydrophobic surface, where water droplets effortlessly roll off, confirming the effective utilization of hydrophobic ZnO NRs for self-cleaning applications.

and weather resistance, ensuring that the coating maintains both optical clarity and hydrophobic performance under repeated use. These combined effects make the ZnO NR/PMMA composite more durable than coatings composed of nanorods alone. The rod-like arrangement of nanorods also introduces microstructural roughness, which, according to Wenzel's model [46], amplifies the intrinsic wetting behaviour of the material. The presence of numerous troughs between nanorods restricts water spreading, resulting in droplet beading and the observed hydrophobicity. While these findings suggest that ZnO NRs could be promising for self-cleaning applications, it should be noted that direct self-cleaning tests (such as roll-off or dust-removal experiments) were not conducted in this study. Nevertheless, the measured hydrophobicity highlights their potential for future self-cleaning surface designs without compromising light transmission (Figure 8C).

Table 1 summarises the hydrophobic properties of the synthesised ZnO NRs and compares them with reported values for similar nanomaterials.

Table 1: Efficacy of the hydrophobicity properties of the synthesized ZnO NRs in comparison to the values for various nanomaterials reported in the literature.

Nanomaterials	Substrate	Contact angle	Bandgap (eV)	Size of nanoparticles (nm)
Tenorite (CuO) [47]	Glass	65.61°	1.21–2.74	13 to 72
Kenaf fiber with ZnO NPs [48]	Fabric	74.40°	–	–
Alumina NPs [49]	Glass slide	22 ± 2	–	13 nm
Silica/alumina nanoparticle mixture [50]	Ceramic alumina disk	158°	–	Average pore size of 0.4 µm
Titanium dioxide nanoparticles (T300) [51]	BK-7 substrates	≈20.82°	3.05	25 nm
ZnO NRs (current study)	Glass	95.6°	2.64 and 3.24	22 nm

3.9 Photodegradation efficiency of ZnO NRs for CV dye under visible light

Figure 9A shows the photodegradation of CV dye in the aqueous phase, facilitated by ZnO nanoparticles under sunlight, in a yard in Al Riyadh city, Saudi Arabia. The CV dye solution, containing ZnO nanorods, exhibited notable and time-dependent degradation, with 95 % ± 0.01 of the colour fading observed within one day of sunlight exposure, as shown in Figure 9B. The effective photocatalytic degradation of CV dye is further demonstrated in Figure 9C. Table 2 presents the performance of the current ZnO NR photocatalysts compared to reported values from previous studies on other nanomaterials as photocatalysts. A comparative analysis of CV dye concentration over irradiation time was conducted. In this context, "C_0" denotes the CV dye concentration before irradiation, while "C" signifies the concentration after irradiation, as shown in Figure 9D. The graphical representation shows a consistent decline in CV dye concentration over time. Using kinetic reaction modelling, the experimental data were analysed to elucidate the photocatalytic behaviour [52].

$$\ln(C/C_0) = \mathrm{Kt} \tag{2}$$

In the above equation, C_0 and C represent the concentrations of CV dye at time zero and at time t, respectively; t denotes the reaction time, and the apparent rate constant is given in min^{-1}. This formulation indicates that the photocatalytic degradation curve follows first-order kinetic behaviour.

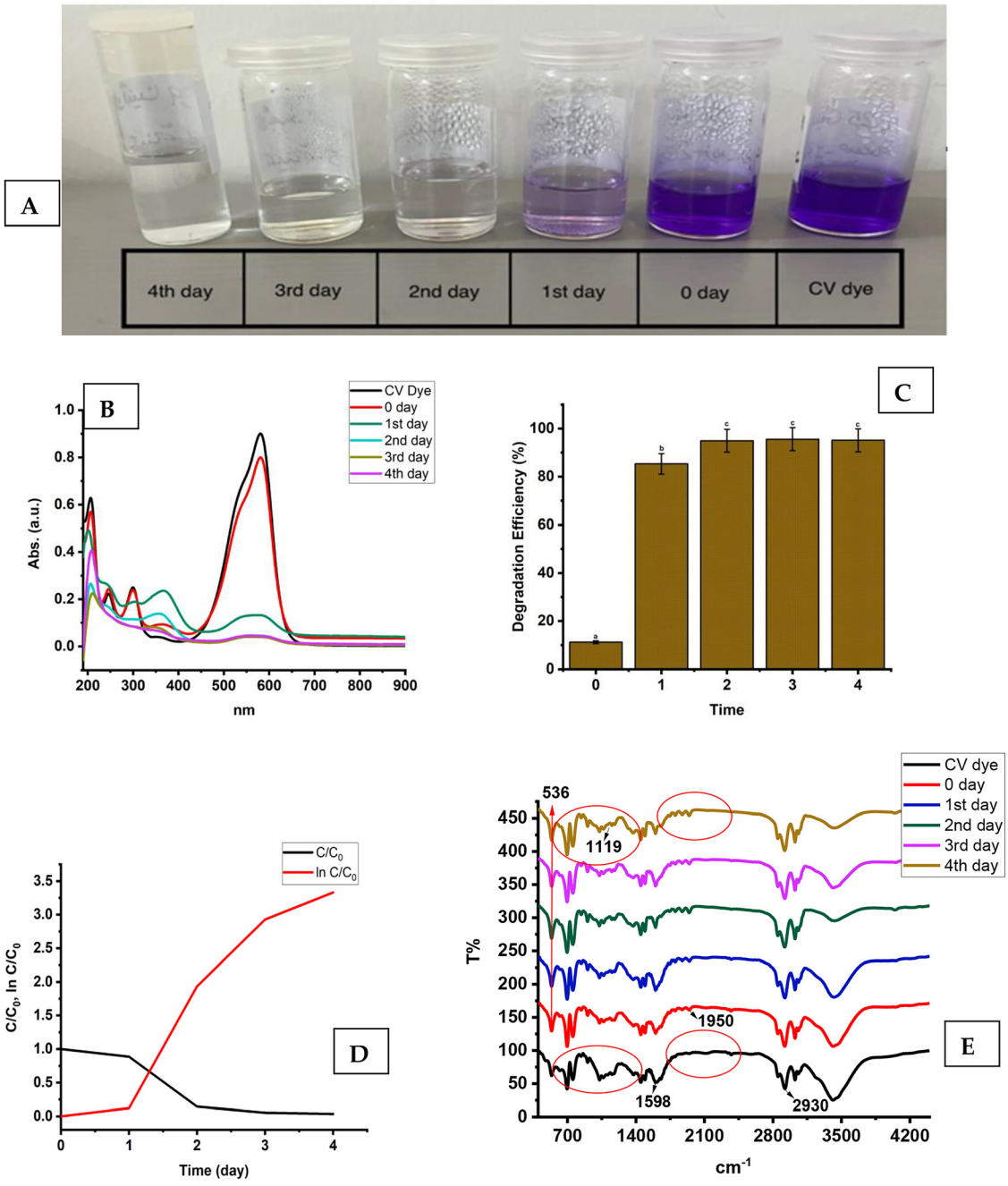

Figure 9: (A) The photodegradation of CV dye over different time durations. (B) The UV–vis spectra of dye photodegradation induced by solar radiation, obtained for CV dye under optimal conditions. (C) The effectiveness of ZnO NRs in degrading CV dye, with different letters (a, b, and c) indicating significant differences at $p > 0.05$. (D) the kinetic plot, including the rate constant and half-life of dye degradation, for the ZnO NR-catalyzed photocatalytic degradation of CV dye. (E) FTIR analysis results of CV dye samples treated with ZnO NRs over varying time durations.

Figure 9D shows the linear relationship between ln (C/C_0) and the irradiation time for CV dye degradation. This relationship yields a rate constant (k) of 0.6767 min^{-1} and a pollutant half-life of 0.959 units for ZnO NRs. To understand the degradation of CV via different processes, we conducted FTIR analysis, with the results presented in Figure 9E. A clear distinction between the FTIR spectra of the degraded dye and the untreated control solution demonstrates substantial degradation of CV induced by ZnO nanoparticles. The FTIR spectra show marked differences in both the fingerprint and

Table 2: The performance of the current photocatalysts – ZnO NRs – in comparison to literature-reported values for different nanomaterials as photocatalysts.

Nanomaterials	Size of nanoparticles (nm)	Photodegradation percentage (%)/Dye	Duration of irradiation	Bandgap (eV)
Cobalt-doped titanium oxide [53]	15–26 nm	90 %/amido black dye	Under UV radiation	–
ZnO NPs [54]	10 nm	99.9 % and 96.8 %/methylene blue and alizarin red S dyes, respectively	UV light irradiation for 100 min	3.19
ZnFe2O4 [55]	21.71 nm	96 %/CV dye	Sunlight for 30 min	1.69–2.55
MnV2O6/BiVO4 heterojunction [56]	32.7–40.1 nm	75 % and 68 %/MB and RhB dyes, respectively	After irradiation with direct sunlight	2.5 eV and 1.60 eV for BiVO4 and MnV2O6, respectively
Zinc oxide-coated biochar nanocomposite [57]	18 nm	92 %/methylene blue dye	Under sunlight irradiation for 0–120 min	2.89 eV
Copper oxide nanoparticles [58]	12.44 nm	65.231 % ± 0.242 and 65.078 % ± 0.392/methyl green and methyl orange, respectively.	Sunlight irradiation for 60 min	Approximately ≈3.8 eV
ZnO NRs – current study	22 nm	95 %/CV dye	Sunlight irradiation for 3 days and daily for 3 h	2.64 and 3.24 eV

functional group regions (3,500–500 cm^{-1}) of the degraded samples compared to the control (CV dye), consistently observed across all degradation processes.

The most prominent peaks in the FTIR spectrum of the untreated sample correspond to mono-substituted and para-disubstituted benzene rings, supporting the peak at 1,598 cm^{-1} attributed to C=C stretching in the benzene ring. Additionally, the peaks at 1,950 cm^{-1} and 2,930 cm^{-1} are associated with C–N stretching vibrations and C–H stretching of the asymmetric CH_3 group, respectively. Notably, the N=N stretching vibration peak at 1,950 cm^{-1} is absent in the FTIR spectrum of the CV dye after treatment with ZnO nanoparticles. This absence suggests changes in the molecular structure, potentially indicating cleavage of the N=N bond during interaction with ZnO nanoparticles. After CV degradation, the region from 1,117 to 534 cm^{-1} is altered, suggesting possible decomposition of aromatic rings. The unchanged Zn–O band at 536 cm^{-1} indicates the structural stability and reusability of ZnO nanorods during photocatalytic degradation [59]. Table 2 compares the photocatalytic performance of ZnO NRs with values for various nanomaterials reported in previous studies. This comparison offers valuable insights into the efficiency of ZnO NRs as photocatalysts and their potential for environmental applications. The materials included were selected based on their reported photocatalytic efficiency, relevance in recent studies, and ability to degrade organic pollutants.

Scheme 1 outlines the reaction mechanisms underlying the degradation properties of ZnO NRs. The degradation of CV dye depends on UV radiation, requiring the elimination of a positive hole (h^+) in the valence band. This process initiates the movement of valence electrons through the conduction band.

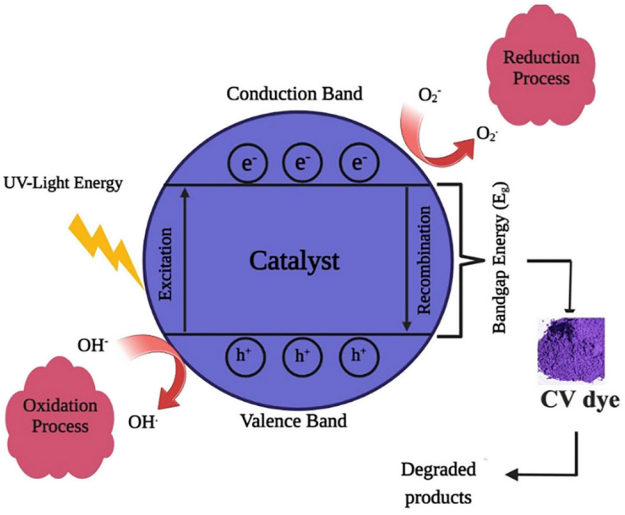

Scheme 1: Reaction mechanisms for the degradation of CV dye using ZnO NRs.

Under UV or sunlight exposure, vacant sites and free electrons interact with absorbed water molecules on the photocatalyst surface, generating OH radicals (OH*). These light-induced radicals play a crucial role in breaking down dye molecules into simpler compounds, such as CO_2 and H_2O. This mechanism is consistent with the findings of [60–63], providing a comprehensive understanding of the photocatalysis process (Equations (3)–(8)).

$$\mathrm{ZnO\ NRs} + h\nu\,(\mathrm{UV}) \rightarrow \mathrm{ZnO\ NRs}\,(e^{-}\,(\mathrm{CB}) + h^{+}\,(\mathrm{VB}))H_2O + h^{+} + (\mathrm{VB}) \rightarrow \mathrm{OH}{+}H^{+} \quad (3)$$

$$O_2 + e^{-}\,(\mathrm{CB}) \rightarrow O2^{-\cdot} \quad (4)$$

$$\mathrm{CV\ dye} + \mathrm{OH}^{\cdot} \rightarrow CO_2 + H_2O \quad (5)$$

$$\mathrm{CV\ dye} + h^{+}\,(\mathrm{VB}) \rightarrow \mathrm{oxidation\ products\ CV\ dye} + e^{-}\,(\mathrm{CB}) \rightarrow \mathrm{reduction\ products} \quad (6)$$

$$\mathrm{CV\ dye} + h\nu \rightarrow \mathrm{CV\ dye}^{*} \quad (7)$$

$$\mathrm{CV\ dye}^{*} + \mathrm{ZnO\ NRs} \rightarrow \mathrm{CV\ dye}^{+} + \mathrm{ZnO\ NRs}^{-} \quad (8)$$

According to the experimental results, the relatively small bandgap of ZnO nanoparticle coatings is responsible for their superior photocatalytic activity. This is because it enables better contact between the coatings and faster electron transfer during the degradation reaction. ZnO nanoparticle coatings have potential for use in self-cleaning coatings and interfaces for occupational and ecological applications, as well as in the light-induced catalytic degradation of organic dyes, due to their strong photocatalytic properties, recyclability, and durability.

4 Conclusions

Zinc oxide nanorods were synthesised using a hydrothermal preparation method, followed by comprehensive characterisation with various analytical techniques, including X-ray diffraction (XRD), Fourier-transform infrared spectroscopy (FTIR), UV-visible spectroscopy, fluorescence spectroscopy (FL), transmission electron microscopy with energy-dispersive X-ray spectroscopy (TEM-EDX), X-ray photoelectron spectroscopy (XPS), and transmittance spectroscopy. XRD analysis confirmed the hexagonal wurtzite structure of ZnO nanorods, with an estimated average crystallite size of approximately 22 nm. UV-visible spectroscopy revealed absorption peaks at 336 nm and 370 nm, corresponding to optical bandgap values of 3.29 ± 0.03 eV and 3.66 ± 0.01 eV, respectively. TEM images showed rod-shaped nanostructures with a width of 47 nm. In photocatalysis tests, the ZnO nanorods exhibited superior photocatalytic activity, particularly in the degradation of crystal violet (CV) dye, attributed to bandgap constriction. Coating experiments demonstrated a photocatalytic decomposition rate constant of 0.6767 min^{-1}, highlighting the material's efficiency and stability. Photodegradation assessments indicated that the ZnO nanorods maintained a degradation efficiency exceeding 95 % ± 0.01, underscoring their excellent photocatalytic performance. The ZnO nanorods also displayed hydrophobic behaviour, with a water contact angle of 95.6° ± 0.3, indicating their suitability for self-cleaning applications. XPS analysis revealed two distinct peaks for zinc, Zn $2p_3/_2$ at ~1,021 eV and Zn $2p_1/_2$ at ~1,044 eV, confirming the presence of ZnO nanorods within the thin film coating on glass slides used for self-cleaning analysis. These results highlight the potential of synthesised ZnO nanorod coatings for environmentally friendly applications, including self-cleaning technologies, with promising capabilities for effectively reducing pollutants and contributing to sustainable environmental solutions. Future studies should evaluate the effectiveness of ZnO nanorods against diverse pollutants and address challenges related to industrial scalability, cost, and reproducibility. Advancing deposition techniques and hybrid materials could further enhance their photocatalytic and self-cleaning properties for broader environmental applications.

Funding information: The authors gratefully acknowledge the financial support from Researchers Supporting Project number (RICSP-25-1), King Saud University, Riyadh, Saudi Arabia.

Author contribution: All authors have accepted responsibility for the entire content of this manuscript and approved its submission.

Conflict of interest: The authors state no conflict of interest.

Data availability statement: All data generated or analysed during this study are included in this published article.

References

1. Saadi H, Khaldi O, Pina J, Costa T, Seixas de Melo JS, Vilarinho P, et al. Effect of Co doping on the physical properties and organic pollutant photodegradation efficiency of ZnO nanoparticles for environmental applications. Nanomaterials 2024;14:122.
2. Madi K, Chebli D, Ait Youcef H, Tahraoui H, Bouguettoucha A, Kebir M, et al. Green fabrication of ZnO nanoparticles and ZnO/rGO nanocomposites from Algerian date syrup extract: synthesis, characterization, and augmented photocatalytic efficiency in methylene blue degradation. Catalysts 2024;14:62.
3. Agarwal H, Kumar SV, Rajeshkumar S. A review on green synthesis of zinc oxide nanoparticles – an eco-friendly approach. Resour Efficient Technol 2017;3:406–13.
4. Rasool A, Sri S, Zulfajri M, Krismastuti FSH. Nature inspired nanomaterials: advancements in green synthesis for biological sustainability. Inorg Chem Commun 2024;169:112954.
5. Senthil RB, Ewe LS, S S, S S, Yew WK, Tiong SK, et al. Recent trends and advancement in metal oxide nanoparticles for the degradation of dyes: synthesis, mechanism, types and its application. Nanotoxicology 2024; 18:272–98.

6. Kaveh R, Alijani H, Falletta E, Bianchi CL, Mokhtarifar M, Boffito DC. Advancements in superhydrophilic titanium dioxide/graphene oxide composite coatings for self-cleaning applications on glass substrates: a comprehensive review. Prog Org Coat 2024;190: 108347.
7. Baig A, Siddique M, Panchal S. A review of visible-light-active zinc oxide photocatalysts for environmental application. Catalysts 2025; 15:100.
8. Kumari H, Sonia S, Ranga R, Chahal S, Devi S, Sharma S, et al. A review on photocatalysis used for wastewater treatment: dye degradation. Water Air Soil Pollut 2023;234:349.
9. Ansari AS, Azzahra G, Nugroho FG, Mujtaba MM, Ahmed ATA. Oxides and metal oxide/carbon hybrid materials for efficient photocatalytic organic pollutant removal. Catalysts 2025;15:134.
10. Chen D, Cheng Y, Zhou N, Chen P, Wang Y, Li K, et al. Photocatalytic degradation of organic pollutants using TiO_2-based photocatalysts: a review. J Clean Prod 2020;268:121725.
11. Varma KS, Tayade RJ, Shah KJ, Joshi PA, Shukla AD, Gandhi VG. Photocatalytic degradation of pharmaceutical and pesticide compounds (PPCs) using doped TiO_2 nanomaterials: a review. Water-Energy Nexus 2020;3:46–61.
12. Qi K, Cheng B, Yu J, Ho W. Review on the improvement of the photocatalytic and antibacterial activities of ZnO. J Alloys Compd 2017; 727:792–820.
13. Khan ME. State-of-the-art developments in carbon-based metal nanocomposites as a catalyst: photocatalysis. Nanoscale Adv 2021;3: 1887–900.
14. Ankita, Rathee, T., Sapana, Chahal S, Kumar S., Kumar A. et al. Growth of advanced oxide nanostructures (nanocubes/nanorods/ nanoflowers). In: Defect-induced magn oxide semiconductors. Cambridge: Woodhead Publishing; 2023, 223:223–44 pp.
15. Rong P, Ren S, Yu Q. Fabrications and applications of ZnO nanomaterials in flexible functional devices – a review. Crit Rev Anal Chem 2019;49:336–49.
16. Laurenti M, Stassi S, Canavese G, Cauda V. Surface engineering of nanostructured ZnO surfaces. Adv Mater Interfaces 2017;4:1600758.
17. Khan MM, Saadah NH, Khan ME, Harunsani MH, Tan AL, Cho MH. Phytogenic synthesis of band gap-narrowed ZnO nanoparticles using the bulb extract of Costus woodsonii. BioNanoScience 2019;9:334–44.
18. Raha S, Ahmaruzzaman M. ZnO nanostructured materials and their potential applications: progress, challenges and perspectives. Nanoscale Adv 2022;4:1868–925.
19. Sharwani AA, Narayanan KB, Khan ME, Han SS. Photocatalytic degradation activity of goji berry extract synthesized silver-loaded mesoporous zinc oxide (Ag@ZnO) nanocomposites under simulated solar light irradiation. Sci Rep 2022;12:10017.
20. Zhu J, Liao K. A facile method for preparing a superhydrophobic block with rapid reparability. Coatings 2020;10:1202.
21. Gao X, Wen G, Guo Z. Durable superhydrophobic and underwater superoleophobic cotton fabrics growing zinc oxide nanoarrays for separation of heavy/light oil and water mixtures. Colloids Surf A Physicochem Eng Asp 2018;559:115–26.
22. Nundy S, Ghosh A, Mallick TK. Hydrophobic and superhydrophobic self-cleaning coatings by morphologically varying ZnO microstructures for photovoltaic and glazing applications. ACS Omega 2020;5:1033–9.
23. Markevich I, Stara T, Khomenkova L, Kushnirenko V, Borkovska L. Photoluminescence engineering in polycrystalline ZnO and ZnO-based compounds. AIMS Mater Sci 2016;3:508–24.
24. Kaningini AG, Azizi S, Sintwa N, Mokalane K, Mohale KC, Mudau FN, et al. Effect of optimized precursor concentration, temperature, and doping on optical properties of ZnO nanoparticles synthesized via a green route using bush tea (Athrixia phylicoides DC.) leaf extracts. ACS Omega 2022;7:31658–66.
25. Manal AA, Hendi A, Ortashi K, Alnamlah R, Alangery A, Ali Alshaya E, et al. Utilizing cymbopogon Proximus grass extract for green synthesis of zinc oxide nanorod needles in dye degradation studies. Molecules 2024;29:355.
26. Alterary SS. Potent and versatile biogenically synthesized alumina/ nickel oxide nanocomposite adsorbent for defluoridation of drinking water. ACS Omega 2024;9:23220–40.
27. Estrada-Urbina J, Cruz-Alonso A, Santander-González M, Méndez-Albores A, Vázquez-Durán A. Nanoscale zinc oxide particles for improving the physiological and sanitary quality of a Mexican landrace of red maize. Nanomaterials 2018;8:247. 195207.
28. Shankar S, Wang LF, Rhim JW. Zinc oxide nanoparticle incorporation improves mechanical, water vapor barrier, UV-light barrier and antibacterial properties of PLA nanocomposite films. Mater Sci Eng C 2018;93:289–98. e202400203.
29. Pudukudy M, Yaakob Z. Facile synthesis of quasi-spherical ZnO nanoparticles with excellent photocatalytic activity. J Cluster Sci 2015; 26:1187–201.
30. Karthikeyan B, Gnanakumar G, Alphonsa AT. Nano metal oxides. Singapore: Springer; 2023.
31. Teke A, Özgür Ü, Doğan S, Morkoç H, Nemeth B, Everitt HO. Excitonic fine structure and recombination dynamics in single-crystalline ZnO. Phys Rev B 2004;70:195207.
32. Podia M, Tripathi AK. Structural, optical and luminescence properties of ZnO thin films: role of hot electrons defining luminescence mechanisms. J Lumin 2022;252:119331.
33. Mascoli V, Bhatti AF, Bersanini L, van Amerongen H, Croce R. The antenna of far-red absorbing cyanobacteria increases both absorption and quantum efficiency of photosystem II. Nat Commun 2022;13:3562.
34. Wang C. Luminescent transition metal complexes: optical characterization, integration into polymeric nanoparticles and sensing applications. Berlin: Freie Universität Berlin; 2021.
35. Bulcha B, Leta Tesfaye J, Anatol D, Shanmugam R, Dwarampudi LP, Nagaprasad N, et al. Synthesis of zinc oxide nanoparticles by hydrothermal methods and spectroscopic investigation of ultraviolet radiation protective properties. J Nanomater 2021;2021:1–10.
36. Javed A, Wiener J, Tamulevičienė A, Tamulevičius T, Lazauskas A, Saskova J, et al. One-step in situ synthesis of zinc oxide nanoparticles for multifunctional cotton fabrics. Materials 2021;14:3956.
37. Awad MA, Hendi AA, Ortashi KM, Alnamlah RA, Alangery A, Alshaya EA, et al. Utilizing cymbopogon proximus grass extract for green synthesis of zinc oxide nanorod needles in dye degradation studies. Molecules 2024;29:355.
38. Nguyen TP, Tan PB, Le T. Effect of poly(vinyl alcohol) (PVA) capping agent on structural, photoluminescent and photometric properties of ZnO nanoparticles. Opt Mater 2022;125:112132.
39. Motelica L, Vasile BS, Ficai A, Surdu AV, Ficai D, Oprea OC, et al. Antibacterial activity of zinc oxide nanoparticles loaded with essential oils. Pharmaceutics 2023;15:2470.
40. Falamas A, Maric I, Nekvapil F, Stefan M, Macavei GS, Barbu-Tudoran L, et al. Surface enhanced fluorescence potential of ZnO nanoparticles and gold decorated ZnO nanostructures embedded in a polyvinyl alcohol matrix. J Photochem Photobiol A: Chem 2023;438:114516.
41. Shakeel N, Piwoński I, Kisielewska A, Krzywiecki M, Batory D, Cichomski M. Morphology-dependent photocatalytic activity of nanostructured titanium dioxide coatings with silver nanoparticles. Int J Mol Sci 2024;25:8824.

42. Meky AI, Hassaan MA, Fetouh HA, Ismail AM, El Nemr A. Hydrothermal fabrication, characterization and RSM optimization of cobalt-doped zinc oxide nanoparticles for antibiotic photodegradation under visible light. Sci Rep 2024;14:2016.
43. Mardosaite R, Jurkeviciute A, Rackauskas S. Superhydrophobic ZnO nanowires: wettability mechanisms and functional applications. Cryst Growth Des 2021;21:4765–79.
44. Althamthami M, Temam HB, Temam EG, Rahmane S, Gasmi B, Hasan GG. Impact of surface topography and hydrophobicity in varied precursor concentrations of tenorite (CuO) films: film properties and photocatalytic efficiency. Sci Rep 2024;14:7928.
45. Mohammed M, Rahman R, Mohammed AM, Betar BO, Osman AF, Adam T, et al. Improving hydrophobicity and compatibility between kenaf fiber and polymer composite by surface treatment with inorganic nanoparticles. Arab J Chem 2022;15:104233.
46. Al-Shatty W, Lord AM, Alexander S, Barron AR. Tunable surface properties of aluminum oxide nanoparticles from highly hydrophobic to highly hydrophilic. ACS Omega 2017;2:2507–14.
47. Huang CY, Ko CC, Chen LH, Huang CT, Tung KL, Liao YC. Simple coating method to prepare superhydrophobic layers on ceramic alumina for vacuum membrane distillation. Sep Purif Technol 2018; 198:79–86.
48. Li Y, Xia B, Jiang B. Thermal-induced durable superhydrophilicity of TiO_2 films with ultra-smooth surfaces. J Sol Gel Sci Technol 2018;87:50–8.
49. Wang W, Lv L, Wang C, Li J. Melamine-assisted thermal activation for vacancy-rich ZnO: calcination effects on microstructure and photocatalytic properties. Molecules 2023;28:5329.
50. Lu J, Ali H, Hurh J, Han Y, Batjikh I, Rupa EJ, et al. Photocatalytic activity assessment of zinc oxide nanoparticles synthesized from Codonopsis lanceolata roots by one-pot green synthesis. Optik 2019; 184:82–9.
51. Abdi M, Balagabri M, Karimi H, Hossini H, Rastegar SO. Degradation of crystal violet using ozone, peroxone, electroperoxone and electrolysis processes: a comparative study. Appl Water Sci 2020;10:1–10.
52. Anitha S, Muthukumaran S. Structural, optical and antibacterial investigation of La- and Cu-doped ZnO nanoparticles synthesized by co-precipitation. Mater Sci Eng C 2020;108:110387.
53. Khan I, Saeed K, Ali N, Khan I, Zhang B, Sadiq M. Heterogeneous photodegradation of industrial dyes: mechanisms and rate-affecting parameters. J Environ Chem Eng 2020;8:104364.
54. Tagnaouti Moumnani F, Khallouk K, Elkhalfaouy R, Moussaid D, Mertah O, Solhy A, et al. Synthesis and characterization of $Zn_3V_2O_8$ nanoparticles: mechanisms and factors influencing crystal violet photodegradation. React Kinet Mech Catal 2024:1–18.
55. Ali I, Alharbi OM, Alothman ZA, Badjah AY. Photodegradation kinetics and thermodynamics of amido black dye over Co/TiO_2 nanoparticles. Photochem Photobiol 2018;94:935–41.
56. Shubha JP, Kavalli K, Adil SF, Assal ME, Hatshan MR, Dubasi N. Green synthesis of ZnO nanoparticles for dye degradation: kinetic modeling approach. J King Saud Univ Sci 2022;34:102047.
57. Bayahia H. High activity of $ZnFe_2O_4$ nanoparticles for sunlight-driven photodegradation of crystal violet dye. J Taibah Univ Sci 2022;16: 988–1004.
58. Bano K, Mittal SK, Singh PP, Kaushal S. Sunlight-driven degradation of organic pollutants using $MnV_2O_6/BiVO_4$ heterojunction photocatalyst. Nanoscale Adv 2021;3:6446–58.
59. Labhane PK, Huse VR, Patle LB, Chaudhari AL, Sonawane GH. Synthesis and characterization of Cu-doped ZnO nanoparticles: optical, FTIR, morphological and photocatalytic study. J Mater Sci Chem Eng 2015;3: 39.
60. Eswaran P, Madasamy PD, Pillay K, Brink H. Sunlight-driven photocatalytic degradation of methylene blue using ZnO/biochar nanocomposite from banana peels. Biomass Convers Biorefinery 2024: 1–21.
61. Aroob S, Carabineiro SA, Taj MB, Bibi I, Raheel A, Javed T, et al. Green synthesis and photocatalytic activity of CuO nanoparticles. Catalysts 2023;13:502.
62. Anaya-Zavaleta JC, Ledezma-Pérez AS, Gallardo-Vega C, Rodríguez-Hernández J, Alvarado-Canché CN, García-Casillas PE, et al. ZnO nanoparticles by hydrothermal method: synthesis and characterization. Technologies 2025;13:18.
63. Karagoz S, Kiremitler NB, Sarp G, Pekdemir S, Salem S, Goksu AG, et al. Antibacterial, antiviral and self-cleaning ZnO/Ag nanofiber mats for protective clothing. ACS Appl Mater Interfaces 2021;13:5678–90.